

# Biomimetic Water-Repelling Surfaces with Robustly Flexible Structures

Songtao Hu, Tom Reddyhoff, Jinbang Li, Xiaobao Cao, Xi Shi,\* Zhike Peng,\* Andrew J. deMello, and Daniele Dini



Cite This: *ACS Appl. Mater. Interfaces* 2021, 13, 31310–31319



Read Online

ACCESS |



Metrics & More



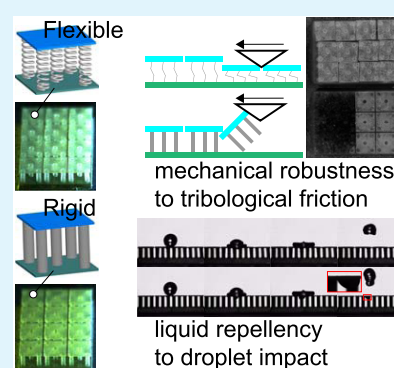
Article Recommendations



Supporting Information

**ABSTRACT:** Biomimetic liquid-repelling surfaces have been the subject of considerable scientific research and technological application. To design such surfaces, a flexibility-based oscillation strategy has been shown to resolve the problem of liquid-surface positioning encountered by the previous, rigidity-based asymmetry strategy; however, its usage is limited by weak mechanical robustness and confined repellency enhancement. Here, we design a flexible surface comprising mesoscale heads and microscale spring sets, in analogy to the mushroomlike geometry discovered on springtail cuticles, and then realize this through three-dimensional projection microstereolithography. Such a surface exhibits strong mechanical robustness against ubiquitous normal and shear compression and even endures tribological friction. Simultaneously, the surface elevates water repellency for impacting droplets by enhancing impalement resistance and reducing contact time, partially reaching an improvement of  $\sim 80\%$  via structural tilting movements. This is the first demonstration of flexible interfacial structures to robustly endure tribological friction as well as to promote water repellency, approaching real-world applications of water repelling.

**KEYWORDS:** biomimetic surface, liquid repellency, friction, droplet transport, 3D printing



Also, a flexibility gradient is created on the surface to directionally manipulate droplets, paving the way for droplet transport.

## 1. INTRODUCTION

Nature provides a wide range of biomimetic surfaces, attracting considerable attention in scientific principles and technological applications, such as liquid-repelling,<sup>1</sup> self-cleaning,<sup>2</sup> droplet manipulation,<sup>3</sup> and energy harvesting,<sup>4</sup> which rely on replicating morphological and chemical attributes of natural surfaces. For liquid-repelling applications, one famous example is the waterproofing surface of the sacred lotus known nowadays as the lotus effect.<sup>5</sup> Due to the inherent advantages imparted by the marriage of hierarchical morphology with wax-based chemical modification, water readily beads up and rolls over the leaf, indicating a high contact angle and low adhesion. In addition to the low-adhesion-generated easy-rolling capability, liquid-repelling surfaces in nature can also trap water droplets due to high adhesion known as the petal effect,<sup>6</sup> which relies on the semiwetting state of their hierarchical morphology between the Wenzel and Cassie–Baxter states. However, these surfaces suffer from a sustained dewetting state and strong repellency to low-surface-tension liquids (i.e., omni-repellency). Fortunately, a promising approach has been discovered in springtail cuticles, with which this widespread arthropod is able to repel most fluorinated liquid so as to guarantee dermal respiration in extremely aqueous environments.<sup>7</sup> Such cuticles have inspired a mushroomlike morphological geometry ranging from singly re-entrant, doubly re-entrant to triply re-entrant topology.<sup>8–16</sup>

In addition to the static repellency above, artificial liquid-repelling surfaces require kinetic repellency against impacting droplets, including strong impalement resistance to rebound droplets and short droplet-surface contact time at impact. Normally, droplets impinging on a super-repellent surface will spread, retract, and bounce off with circular symmetry, resulting in the contact time bounded below by an inertia-capillarity limit.<sup>17</sup> Accordingly, interfacial features with macro curvatures have been created to break the symmetry, leading to impalement resistance enhancement and contact time reduction owing to the asymmetrical droplet dynamics at impact.<sup>18–22</sup> Recently, natural leaves and wings have inspired another strategy that abandons the conventional rigid prerequisite. In comparison to the asymmetry mechanism followed by rigid surfaces, flexible surfaces promote kinetic repellency by reducing impacting loads through their oscillations,<sup>23–25</sup> extending the related research from statics to dynamics.

Despite this, both the rigidity-based asymmetry mechanism and the flexibility-based oscillation mechanism require strict

Received: June 1, 2021

Accepted: June 14, 2021

Published: June 25, 2021



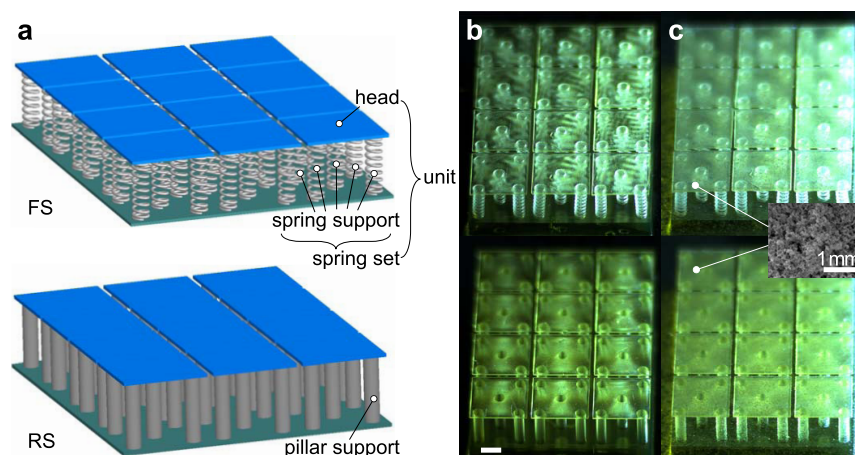


**Figure 1.** Flexible and rigid surfaces. (a) Design of the flexible surface FS as a matrix of singly re-entrant mushroomlike units, each unit comprising a square head and a spring set consisting of five springlike flexible supports, in reference to the rigid surface RS with pillarlike rigid supports. (b, c) Optical microscopy images of fabricated surfaces using three-dimensional projection microstereolithography and low-surface-energy chemical modification. Scale bar: 1 mm.

impacting positioning, thereby limiting their usage. Consequently, the use of flexible interfacial microstructures, instead of entire surface flexibility, has been proposed to cope with the positioning problem,<sup>26–28</sup> due to the great structural uniformity in micro-nano fabrication. Differing from a needlelike flexible microstructure utilizing bending movements at droplet impact,<sup>27,28</sup> the mushroomlike microstructure has substituted its pillarlike rigid support with a springlike flexible one.<sup>26</sup> Such a microstructure is, however, criticized for weak mechanical robustness (tribological friction under  $\sim 0.04 \text{ N mm}^{-1}$ ) and limited repellency enhancement ( $\sim 15\%$ ).<sup>26,29</sup>

Here, we report a water-repelling biomimetic surface structured with singly re-entrant mushroomlike basic units through three-dimensional projection microstereolithography, each unit comprising a mesoscale head and a microscale spring set. Such a surface exhibits high recovery capability in response to ubiquitous normal and shear compression, even to achieve strong mechanical robustness against tribological friction under  $\sim 0.44 \text{ N mm}^{-1}$ . Simultaneously, the flexibility of underlying spring sets is shown to elevate the kinetic repellency in relation to droplet intrusion in terms of impalement resistance enhancement and contact time reduction, partially reaching an improvement of  $\sim 80\%$  via structural tilting movements. We believe this study to be the very first demonstration of flexible interfacial structures to robustly endure tribological friction as well as to promote water repellency, which approaches real-world applications of water repelling. In addition, by designing nonuniform spring sets to create a flexibility gradient, the surface is able to directionally manipulate droplets, thus paving the way for droplet transport.

## 2. EXPERIMENTAL SECTION

**2.1. Surface Fabrication.** Three-dimensional projection microstereolithography was conducted on nanoArch S140 (BMF Precision Technology Co Ltd., China) to cure the commercially available HTL photosensitive resin (BMF Precision Technology Co Ltd., China), fabricating the designed surfaces on ITO-coated fused silicas. Commercial low-surface-energy particles, Ultra-Ever Dry (Ultra Tech International Inc), were sprayed to the printed surfaces, coupling chemical modification.

**2.2. Morphology Characterization.** Morphological images of surfaces were taken with an optical microscope LW300LMDT (Cewei Guangdian, China).

**2.3. Compression Test.** Tweezer was used to compress mushroomlike flexible units normally and tangentially on an optical microscope LW300LMDT (Cewei Guangdian, China). The load–displacement relation of mushroomlike flexible units was measured on a tensile-pressure tester ZQ990A (ZHIQU Precision Instruments, China) in pressure mode. The measurement was repeated three times for repeatability.

**2.4. Friction Test.** Tribological friction was conducted by loading and sliding a triangular rubber wiper against the fabricated surfaces on a self-built tribological test rig. On the tester, the surfaces were stationary held as the lower specimen, while the wiper had a controlled movement as the upper specimen (see Figure S1). The wiper was declined to approach a line contact with the surfaces at a normal load of 1, 2, or 4 N and was then slid over the surface at a speed of  $1 \text{ mm s}^{-1}$ . The frictional and normal loads were recorded at a step of 0.1 s to yield the ratio known as the coefficient of friction.

**2.5. Static Repellency Test.** Static repellency of surfaces was investigated on a contact-angle goniometer SDC-100 (SINDIN, China) in sessile drop mode under controlled temperature ( $25 \text{ }^\circ\text{C}$ ) and relative humidity (45%). The fabricated surfaces were controlled to lightly contact, heavily contact, and slide over hanging  $2 \mu\text{L}$  of deionized water droplets. To measure the contact angle,  $2 \mu\text{L}$  of deionized water droplets were dropped from a micropipette at a low velocity. The measurement was conducted 30 s after the droplets contacted the surfaces to ensure equilibrium. Three measurements were repeated for each surface for repeatability.

**2.6. Kinetic Repellency Test.** Impacting behaviors of  $8 \mu\text{L}$  of deionized water droplets on the fabricated surfaces were recorded by a high-speed camera FASTCAN SA1.1 (Photron USA Inc) at a rate of 5000 fps. An electrically controlled microsyringe pump was used to release droplets at a specified height. Three measurements were repeated for each surface at each releasing height for repeatability. Specifically, for the oblique droplet impact, the surface holder was tilted with an angle of  $35^\circ$ .

## 3. RESULTS AND DISCUSSION

**3.1. Design and Fabrication.** We designed a flexible surface FS as a matrix of singly re-entrant mushroomlike basic units, each unit comprising a mesoscale square head and a spring set consisting of five microscale springlike flexible supports (see Figure 1a). These mushroomlike units were prescribed in a rectangular array with a pitch of  $3000 \mu\text{m}$ . The length and thickness of the heads were set to 2800 and  $100 \mu\text{m}$ , respectively. Each head had one support at the center and four supports near the corners with a distance of  $2000 \mu\text{m}$ . For each springlike

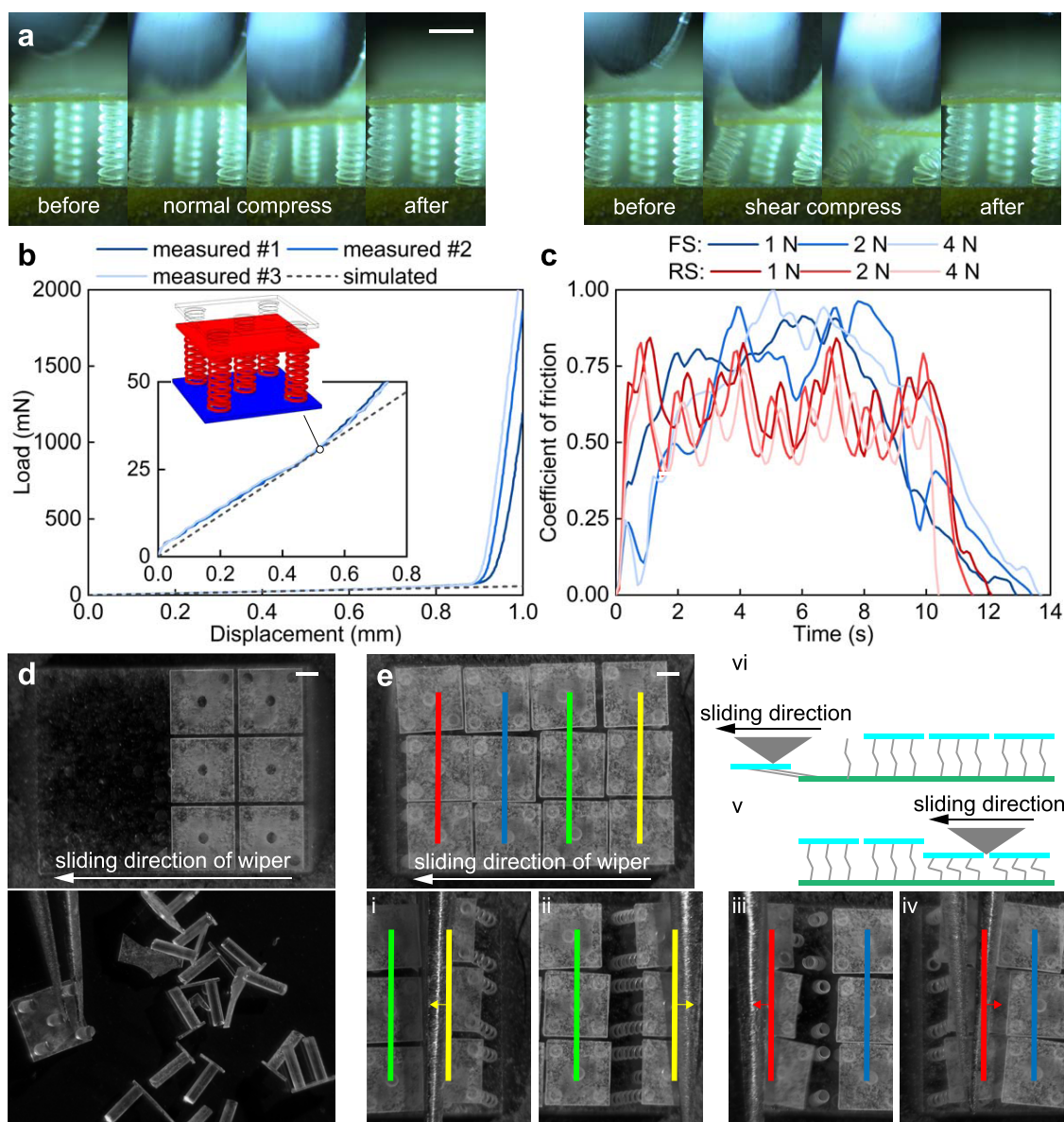


**Figure 2.** Mechanical robustness of mushroomlike units. (a) Mechanical robustness of mushroomlike flexible units against normal and shear compress on an optical microscope. (b) Mechanics of mushroomlike flexible units by measuring the load–displacement relation on a tensile-pressure tester, in comparison to mechanics simulation. (c) Mechanical robustness of mushroomlike units against tribological friction at a normal load (1, 2, or 4 N) and a sliding speed of  $1 \text{ mm s}^{-1}$ . (d) Rigid surface RS after friction under 4 N. (e) Flexible surface FS after friction under 4 N. Scale bar: 1 mm.

support, the free height and mean diameter were set to 2000 and  $500 \mu\text{m}$ , respectively, and the coil number and coil diameter were set to 8 and  $90 \mu\text{m}$ , respectively. Three-dimensional projection microstereolithography was conducted on the nanoArch S140 system (BMF Precision Technology Co Ltd., China) to realize our design (see Figure 1b) because it has been proven as an industrial microprecision printer to rapidly tailor stereostructures for liquid repellency.<sup>30,31</sup> Although the FS was purposely designed as a matrix consisting of  $3 \times 4$  units due to the block size of the printer ( $19.2 \times 10.8 \text{ mm}^2$ ), it would be simple to extend the size via splicing for any industrial application. During structural modeling and fabricating, there was a tradeoff between structural rigidity and flexibility. We initially designed the supports as different zigzag springs to guarantee strong mechanical robustness (see Figure S2a) regardless of the flexibility to trigger structural oscillations at droplet impact. Then, returning to common cylinder helix

springs, a parametric discussion was conducted to avoid excessive flexibility, which can yield inclined and collapsed behaviors (see Figure S2b). As per previous studies, the singly re-entrant mushroomlike geometry can repel impinging droplets solely from the morphological point of view,<sup>9,13,15,29</sup> we, however, sprayed the FS with low-surface-energy particles to couple chemical modification (see Figure 1c)<sup>1</sup> because in this study we mainly focused on the kinetic repellency under extremely impacting conditions. As a reference, we designed and fabricated the corresponding rigid surface (RS) with springlike flexible supports substituted with pillarlike rigid ones. Also, we designed and fabricated a smooth surface SS (see Figure S3).

**3.2. Mechanical Robustness.** To test mechanical robustness,<sup>1,14,32–34</sup> we first compressing the FS by a tweezer on an optical microscope (see Figure 2a and Movie S1). For a mushroomlike flexible unit, springlike supports deformed downwards when the head was normally compressed, but

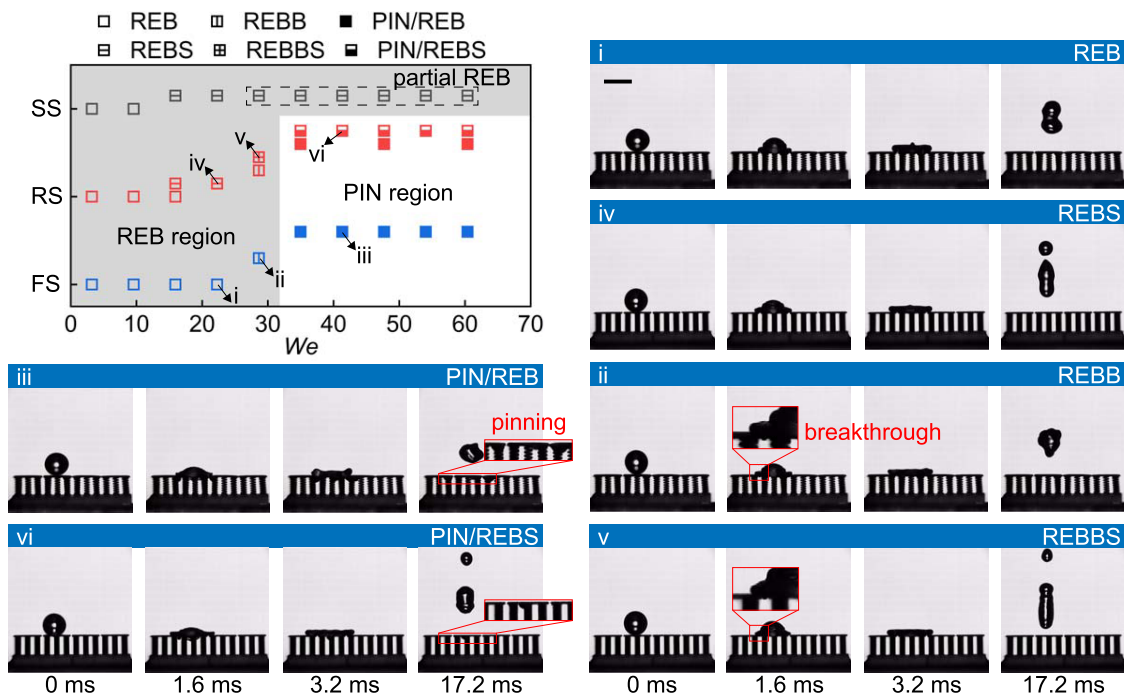


**Figure 3.** Kinetic impalement resistance of mushroomlike units. Outcomes of water droplets normally impacting mushroomlike units as a function of  $We$ . Snapshots exemplarily provided to visualize different outcomes over time, including rebounding (REB, i), segmental rebounding (REBS, iv), rebounding with breakthrough (REBB, ii), segmental rebounding with breakthrough (REBBS, v), pinning with rebounding (PIN/REB, iii), and pinning with segmental rebounding (PIN/REBS, vi). Scale bar: 3 mm.

rapidly recovered after releasing the load. The recovery capacity remained even when the head was sheared, thus demonstrating the good mechanical robustness endowed by the flexible supports in response to normal and shear compression that is unavoidable in daily use. To quantify mechanical properties, we experimentally captured the load–displacement relation by compressing the mushroomlike flexible unit with a spherical indenter on a tensile-pressure tester (see Figure 2b). Also, we evaluated the load–displacement relation by finite element simulation analyses in COMSOL Multiphysics (COMSOL Inc, U.K.) with the elasticity modulus, Poisson ratio, and density of 4.5 GPa, 0.35, and  $1100 \text{ kg m}^{-3}$ . One inset was provided to visualize simulation analyses. For the simulated relation, a moderate slope gave a clear indication that the supports were flexible enough to follow a linear response against the applied normal load, respecting Hooke's law. However, due to the structure interference, the measured relations rendered a rapid increase when the head displacement exceeded  $\sim 0.6 \text{ mm}$ , which can be regarded as the allowable amplitude of oscillation for the mushroomlike flexible unit. Within the linear region, the measured load was higher than the simulated one at the same displacement, which can be ascribed to the presence of low-surface-energy particles. Of note, the measurement was repeated three times, showing good repeatability.

We further explored the mechanical robustness with regard to a real-world scenario, i.e., tribological friction. A triangular rubber wiper was declined to approach a line contact with the FS at a normal load (1, 2, or 4 N) and was then slid over the surface at a speed of  $1 \text{ mm s}^{-1}$  (see Figure S1). As a reference, friction tests were also carried out on the RS. During the sliding, the interaction between the frictional pair produced a shear load, yielding the coefficient of friction as the ratio between the shear and normal loads (see Figure 2c). The coefficient of friction for the RS rose up to a stable value around  $\sim 0.6$  and then declined

to zero, with some fluctuations in the stable stage due to the gaps between adjacent mushroomlike units. In comparison to the cases under 1 and 2 N, the coefficient of friction under 4 N was the first to reach zero because of the generation of structural damage (see Figure 2d). The damage can be classified into breakages at pillar-bottom connections and head fragmentations.

The same trend was presented by the coefficient of friction for the FS. However, the increasing and decreasing slopes were milder than those of the RS, which can be ascribed to the bending behaviors of springlike supports under shear loads (see Figure 2a). The larger the applied normal load, the milder the slope. The bending behaviors also produced a higher stable value (even transiently reaching  $\sim 1.0$ ) in comparison to the RS, implying a more severe frictional state owing to the structural compliance. The structural damage was evidenced under 4 N by tracking the status of mushroomlike units after friction (see Figure 2e). Although no fragmentation was directly observed on irregularly patterned heads, some breakages can be found at spring-head connections by shearing the heads with a tweezer (i–iv). Herein, different color stripes were used to position the subimages (i–iv) referring to Figure 2e; and the arrows were used to denote the shearing direction of the tweezer. Of note, these spring-head breakages only occurred on one side of the mushroomlike units at the end of the friction (iii). For the former mushroomlike units, two adjacent units can share the load from the sliding wiper (v); however, the last mushroomlike unit had to support the wiper load through the extreme extension of its springlike supports, resulting in spring-head breakages (vi). Even if the FS and RS started to exhibit structural damage under the same normal load of 4 N, the ratio of damaged units on the FS was lower than that on the RS. Also, nonfragmented heads on the FS, to an extreme, retained water repellency due to the intact mushroomlike geometry. Gratify-

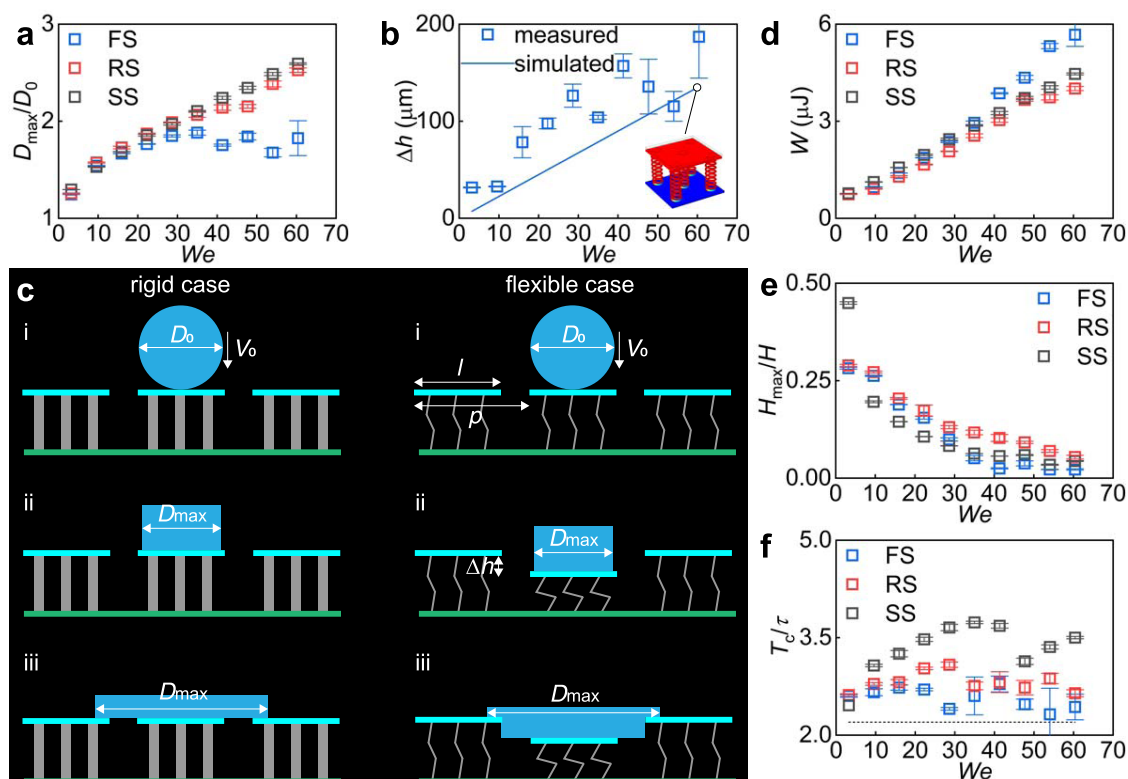


**Figure 4.** Droplet dynamics impacting mushroomlike units. (a) Maximum spreading factor  $D_{\max}/D_0$  of water droplets as a function of  $We$ . (b) Maximum displacement  $\Delta h$  of mushroomlike flexible units as a function of  $We$ , in comparison to mechanics simulation. (c, d) Theoretical spreading model to estimate the work done  $W$  of water droplets in spreading and the results as a function of  $We$ . (e) Restitution coefficient  $H_{\max}/H$  of water droplets as a function of  $We$ . (f) Dimensionless contact time  $T_c/\tau$  as a function of  $We$ , together with the theoretical inertia-capillarity limit  $T_c/\tau = 2.2$ .

ingly, mushroomlike microstructures in previous studies presented structural damage in friction tests with the normal pressure as low as  $0.04 \text{ N mm}^{-1}$ ,<sup>29</sup> criticizing the weak mechanical robustness. Here, our mushroomlike structures started to exhibit structural damage under the normal pressure of  $\sim 0.44 \text{ N mm}^{-1}$ , thereby confirming a greater ( $\sim 11$  times) mechanical robustness against tribological friction to approach real-world applications.

**3.3. Static Repellency.** We investigated the static repellency of the fabricated surfaces by lightly contacting, heavily contacting, and sliding over hanging water droplets on a contact-angle goniometer (see [Movie S2](#)). When the mushroomlike unit on the FS or the RS lightly touched the droplet (see [Figure S4a](#)), the droplet beaded up and eventually left the unit, indicating high contact angle and low adhesion, which can also be evidenced by the smooth movement when the unit slid over the droplet. Under the heavy-contact condition, the droplet preferred to climb up along the microsyringe needle rather than spreading on the unit, again highlighting the great static repellency. During the contacting and sliding, no structural deformation was observed on the FS owing to its mechanical robustness discussed above. Similarly, the same phenomena can be found when the gap between two adjacent mushroomlike units lightly contacted, heavily contacted, and slid over hanging droplets (see [Figure S4b](#)), demonstrating the great repellency in response to static liquid.

We further quantified the values of the contact angle by dripping water droplets from a micropipette at a low velocity since a hanging droplet cannot be directly trapped by these waterproofing surfaces. Owing to low adhesion, the dripping droplet rolled and eventually rested at the center of a gap cross

within  $2 \times 2$  mushroomlike units. The FS and RS exhibited contact angles of  $142.03$  and  $142.60^\circ$  that were smaller than the value of  $154.03^\circ$  measured on the SS, thus indicating an underestimation as the droplet rested at the center of a gap cross (see [Figure S5](#)). Also noteworthy are the nearly equal contact-angle values when the surfaces changed from rigidity to flexibility. Generally speaking, a smaller contact angle can be characterized on a flexible surface than a rigid one because the contact angle is a macroscopic evaluation index based on a specified baseline so that the deformation of the flexible surface arising from the droplet gravity will identify a reduced value to underestimate the real static repellency.<sup>26</sup> However, thanks to the good mechanical robustness, the absence of structural deformation on the FS ensured an accurate contact-angle characterization.

**3.4. Kinetic Repellency of Mushroomlike Units.** To study kinetic repellency, we conducted impacting tests on the fabricated surfaces with water droplets impacting mushroomlike units at different velocities (see [Movie S3](#)). [Figure 3](#) shows the outcomes of impacting events along with an increased Weber ( $We$ ) number (see [Table S1](#)). Here,  $We$  is a nondimensionalized index expressed by  $D_0\rho V_0^2/\sigma$  to quantify the ratio between inertial and capillary loads;  $D_0$  and  $V_0$  are the droplet diameter and velocity before impact; and  $\rho$  and  $\sigma$  are the droplet density and tension. Referring to the definitions of the Wenzel and the Cassie–Baxter wetting states, we defined the outcomes of the FS as follows. For the rebounding, the impinging droplet spread, retracted, and eventually bounced off the mushroomlike units (i and ii). The rebounding behavior can be classified into two types: at small  $We$  (REB; i), the droplet cannot impale the defense of the heads because the impacting load was smaller

than the breakthrough limit;<sup>9,10</sup> at large  $We$  (REBB; ii), as the impacting load slightly exceeded the breakthrough limit, the droplet impaled the heads but eventually bounced off. Here, B stands for the breakthrough of the impaled droplet. Of course, when the value of  $We$  continued to rise up (PIN/REB; iii), the pinning behavior inherited the place of the rebounding, where the droplet impaled the heads and then touched the supports or the substrate so that the lower part was trapped by the mushroomlike units while the upper part was rebounded. Referring to previous studies, the PIN/REB behavior can be termed as partial rebounding. However, in this study, the partial rebounding has been regarded as the failure of impalement resistance.<sup>25</sup> Similar outcomes can be observed on the RS but exhibited three special extensions, including REBS (iv), REBBS (v), and PIN/REBS (vi), where S stands for the segmentation of the rebounded droplet. More precisely, the rebounded droplets (iv and v) or the rebounded droplet part (vi) was segmented into the upper and lower satellites.

The FS and RS exhibited the synchronous occurrence of REBB(S)-to-PIN/REB(S) transformation at  $We$  of  $\sim 34.98$ , indicating the same kinetic impalement resistance. This appears to violate the impalement resistance enhancement endowed by the surface flexibilization in previous studies.<sup>23–28</sup> By checking impalement behaviors (see Movie S3), one cause of the conflict was eventually discovered. The impacted mushroomlike unit normally oscillated to reduce the impacting load, elevating kinetic impalement resistance; however, the structural downward movement also helped the horizontal movement (see Figure S6) of the impaled droplet due to the capillary force, resulting in the negative effect on kinetic impalement resistance. This paves the way for the further structural optimization of mushroomlike units by changing the singly re-entrant heads into doubly re-entrant ones. Of note, the SS started to exhibit a partial REB when  $We$  exceeded  $\sim 22.27$  (see Figure S7), which can be regarded as impalement resistance failure referring to previous works.<sup>25</sup>

Also, we discussed the droplet dynamics in terms of spreading performance, restitution coefficient, and contact time (see Figure 4). Figure 4a shows the maximum spreading factor  $D_{\max}/D_0$  of water droplets as a function of  $We$ , where  $D_{\max}$  is the maximum droplet diameter. In the rebounding region ( $We < 34.98$ ), the FS exhibited a smaller  $D_{\max}/D_0$  than the RS, in consistent with the findings in previous studies.<sup>23–28</sup> As per these studies, when the natural frequency of the flexible surface is lower than that of the droplet, the downward motion of the surface will proceed throughout the whole spreading phase of the droplet, thus reducing impacting load to reduce  $D_{\max}/D_0$  in comparison to the rigid case. Alternatively, the flexible surface will reach the maximum deformation before the droplet spreads to the maximum diameter, resulting in a mild  $D_{\max}/D_0$  reduction that is not solely ascribed to the reduction of impacting load but also the viscoelastic breaking effect of soft materials.<sup>35</sup> By characterizing the maximum displacement  $\Delta h$  when water droplets impacted the mushroomlike flexible units at the edge of the FS (see Figure S8 and Movie S4), we confirmed that the impacted mushroomlike flexible unit reached the maximum downward movement before the droplet spread thoroughly, denoting the second explanation above. In the pinning region ( $We \geq \sim 34.98$ ), the value of  $D_{\max}/D_0$  continued to rise on the RS but began to decrease on the FS as  $We$  increased. For the FS, besides the reduction of impacting load and the viscoelastic breaking effect, the downward movement of the impacted mushroomlike flexible unit also benefited the droplet impale-

ment, thereby decreasing the rebounded droplet to further reduce  $D_{\max}/D_0$ .

Based on momentum conservation, the maximum impacting load can be expressed by  $0.25\pi\rho D_0^2 V_0^2$ , denoting an impacting pressure  $\rho V_0^2$  applied over an area  $0.25\pi D_0^2$ ,<sup>36</sup> which has been demonstrated by the impacting images obtained every 0.2 ms (see Figure S8). Accordingly, we evaluated the maximum displacement  $\Delta h$  of the FS at droplet impact by simulation analyses, and then compared with the measured value (see Figure 4b). One inset was provided to visualize the simulation analyses. The measured  $\Delta h$  was lower than the simulated one at the same  $We$ , which can be ascribed to the larger mechanical stiffness arising from low-surface-energy particles (see Figure 2b).

With a view to further study how the flexibility can affect droplet spreading, we established a theoretical model based on energy conservation to estimate the work done  $W$  (see Figures 4c and S9). For the rigid case,  $W$  is expressed by

$$W = W_k + W_s + W_p$$

$$\begin{cases} W_k = \frac{\pi\rho D_0^3 V_0^2}{12} \\ W_s = \pi\sigma\left(D_0^2 - D_{\max}^2 \frac{1 - \cos\theta}{4}\right) \\ W_p = \frac{\pi\rho g D_0^3}{6} \left(\frac{D_0}{2} - \frac{D_0^3}{3D_{\max}^2}\right) \end{cases} \quad (1)$$

and for the flexible case,  $W$  is rendered as

$$W = W_k + W_s + W_p$$

$$\begin{cases} W_k = \frac{\pi\rho D_0^3 V_0^2}{12} \\ W_s = \pi\sigma\left(D_0^2 - D_{\max}^2 \frac{1 - \cos\theta}{4}\right) \\ W_p = \frac{\pi\rho g D_0^3}{6} \left(\frac{D_0}{2} - \frac{D_0^3}{3D_{\max}^2} + \Delta h\right) - \frac{k\Delta h^2}{2} \\ \quad \text{if } D_{\max} < 2p - l \\ W_p = \frac{\pi\rho g D_0^3}{6} \left(\frac{D_0}{2} - \frac{D_0^3(1 - \alpha)^2}{3D_{\max}^2} + \frac{\alpha}{2}\Delta h\right) \\ \quad - \frac{k\Delta h^2}{2} \quad \text{if } D_{\max} \geq 2p - l \\ \text{where } \alpha = \frac{6(2p - l)^2 \Delta h}{\pi D_0^3} \end{cases} \quad (2)$$

where  $\theta$  is the apparent contact angle,  $g$  is the gravitational acceleration,  $\alpha$  is the mass ratio,  $l$  is the head length,  $p$  is the head pitch, and  $k$  is the stiffness of the mushroomlike flexible unit. Using this model, we evaluated the work done (see Figure 4d), where the value of  $k$  was captured from the established load–displacement relation (see Figure 2b). The work done monotonically increased along with the increased  $We$ , corresponding to the intensified droplet impalement and energy consumption. The spreading droplets dissipated more energy on the FS than on the RS. With regard to the FS, the rigid model

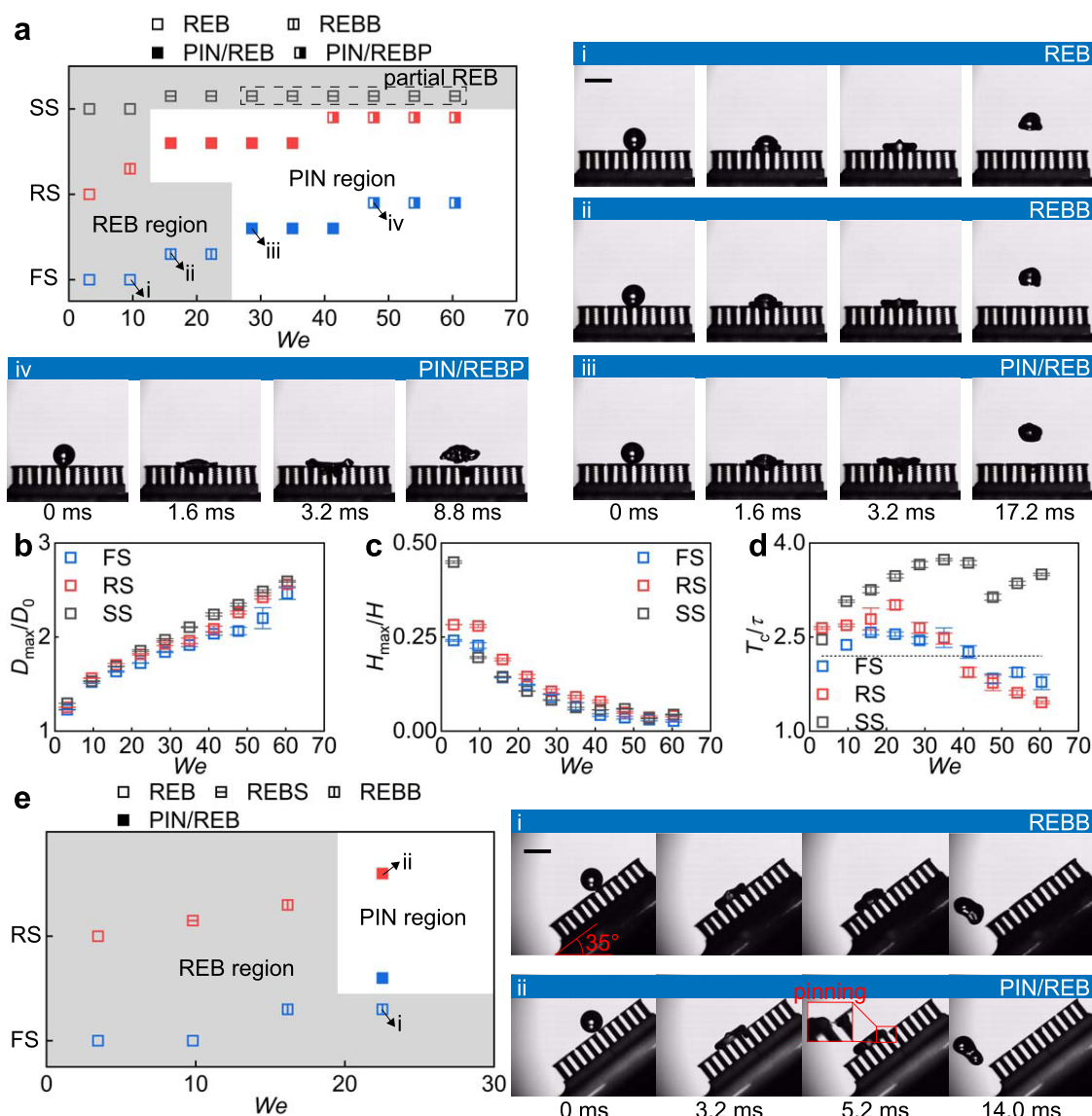


**Figure 5.** Kinetic repelling of gaps between mushroomlike units. (a) Kinetic impalement resistance of mushroomlike units as a function of  $We$ , with water droplets normally impacting the gaps. Snapshots exemplarily provided to visualize different outcomes over time, including rebounding (REB, i), rebounding with breakthrough (REBB, ii), pinning with rebounding (PIN/REB, iii), and pinning with pancakelike rebounding (PIN/REBP, vi). (b) Maximum spreading factor  $D_{max}/D_0$  of water droplets as a function of  $We$ . (c) Restitution coefficient  $H_{max}/H$  of water droplets as a function of  $We$ . (d) Dimensionless contact time  $T_c/\tau$  as a function of  $We$ , together with the theoretical inertia-capillarity limit  $T_c/\tau = 2.2$ . (e) Tilting movements of mushroomlike flexible units to repel obliquely impacting water droplets with an angle of  $35^\circ$ . Scale bar: 3 mm.

overstated the energy consumption in comparison to the flexible model.

Figure 4e shows the restitution coefficient  $H_{max}/H$  as a function of  $We$ , where  $H$  is the releasing height and  $H_{max}$  is the maximum bouncing height. This coefficient is an index to quantify the energy eventually remaining in the rebounded droplet regardless of mass loss at impact. The value of  $H_{max}$  is characterized as the distance from the top side of the head to the lowermost rim of the rebounded droplet (or the larger satellite in a segmental bouncing case). Consistent with the above discussion on work done, the increased  $We$  indicated the increased droplet impalement and energy consumption, leading to the decreased restitution coefficient, and the FS exhibited smaller restitution coefficients than the RS owing to greater energy consumption.

Figure 4f shows the nondimensionalized contact time  $T_c/\tau$  as a function of  $We$ , where  $\tau$  is a timescale expressed by

$(0.125\rho D_0^3/\sigma)^{0.5}$ .<sup>17</sup> The dashed line denotes the theoretical limit of 2.2 by balancing inertial and capillary forces. The FS and RS exhibited an obvious reduction in comparison to the SS. As  $We$  increased, the FS showed a reduced contact time in comparison to the RS with an increased deviation. However, this reduction was interrupted by the occurrence of droplet pinning at  $We \sim 34.98$ . In the pinning region ( $We \sim 34.98$ ), the contact time in the FS or the RS case began to fluctuate along with the increased  $We$ , which can be ascribed to a stick-slip effect. More precisely, the pinning of the impaled portion of the droplet delayed the bouncing of the rebounded portion, yielding an increased contact time; the above delay increased as the partial pinning behavior intensified with increasing  $We$ ; when  $We$  continued to rise up, the impaled portion became large enough in relation to the rebounded part, helping the rebounded portion to reversely shorten the contact time; the above steps were repeated to yield the fluctuant contact time as a function of  $We$ .

This stick-slip effect can be used to explain the fluctuation of contact time on the SS along with the increased  $We$ , owing to the existence of partial rebounding.

**3.5. Kinetic Repellency of Gaps between Mushroomlike Units.** Besides mushroomlike units themselves, we investigated the kinetic repellency of the fabricated surfaces by impacting water droplets on the gaps between two adjacent mushroomlike units at different velocities (see *Movie S5*). *Figure 5a* shows the outcomes of impacting events as a function of  $We$  (see *Table S1*). Similar to the outcomes of droplet-unit impact, either the FS or the RS changed from the REB (i) to the REBB (ii), and eventually entered into the PIN/REB (iii) as  $We$  increased. However, when the value of  $We$  continued to rise up, the PIN/REB transformed into the PIN/REBP (iv), where the impaled droplet portion was still trapped by mushroomlike units while the rebounded droplet exhibited a pancakelike shape.<sup>25,37</sup> Of note, this pancake shape usually denotes a bouncing droplet with uncompleted retraction, implying an obvious contact time reduction, which will be verified later. Gratifyingly, the FS exhibited the REBB-to-PIN/REB transformation at  $We$  of  $\sim 28.62$ , higher than the value of  $\sim 15.92$  in the RS case, indicating a 79.77% enhancement of kinetic impalement resistance. By tracking the dynamics of water droplets when they impacted the unit gaps at the edge of the FS (see *Movie S6*), the mechanism was discovered as below. The mushroomlike flexible unit oscillated at droplet impact to reduce the impacting load, elevating kinetic impalement resistance. Moreover, as the impact occurred on the gap between two adjacent mushroomlike flexible units, only one side of the head endured the impacting load for each unit, thus tilting the head (see *Figure S10*). The tilting movements of the two mushroomlike flexible units prevented the horizontal movement of impaled droplets caused by the capillary force (see *Figure S11*), further elevating kinetic impalement resistance.

Also, we investigated the droplet dynamics in terms of spreading performance, restitution coefficient, and contact time (see *Figure Sb–d*). Similar to the droplet-unit impact, the FS exhibited smaller maximum spreading factors, lower restitution coefficients, and shorter contact time in comparison to the RS. Differently, when the value of  $We$  was large enough, the stick-slip phenomenon of contact time was absent. As mentioned in droplet outcomes, the occurrence of pancake bouncing indicated droplet takeoff with uncompleted retraction so as to reduce contact time remarkably. The larger the value of  $We$ , the more obvious the pancake shape, resulting in shorter and shorter contact time. Also noteworthy is the reversed relation of contact time between the FS and RS cases. Because the impacting load was reduced by the structural oscillations on the FS, the pancake bouncing was earlier to appear and more serious on the RS, eventually making the contact time in the RS case shorter than that in the FS case.

We further applied the findings of angular tilting of mushroomlike flexible units to repelling obliquely impacting water droplets with an angle of  $35^\circ$  (see *Movie S7*). *Figure 5e* shows the outcomes of impacting events as a function of  $We$  (see *Table S1*). The RS changed from the REB(S) to the REBB and eventually entered into the PIN/REB (ii) at  $We$  of  $\sim 22.51$ . Under the same conditions, the FS still remained the REBB response (i) to impinging droplets, highlighting the greater kinetic impalement resistance induced by structural tilting movements.

**3.6. Droplet Transport.** In addition, we designed and fabricated other artificial surface comprising mushroomlike

flexible units, each unit having a spring set mixing with two types of microscale springlike supports (see *Figure 6*). They had the

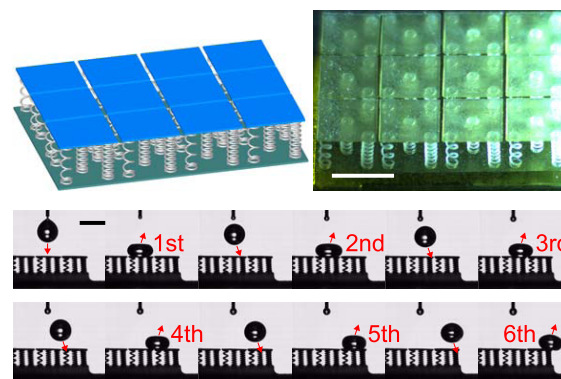


**Figure 6.** Flexibility combination in mushroomlike units to create a flexibility gradient for directional droplet transport. Scale bar: 3 mm.

same structural parameters except for the coil number, i.e., 4 or 8. Such a flexibility combination within each unit created a flexibility gradient, benefiting the directional manipulation of impinging droplets. After releasing, the water droplet bounced six times and eventually left the surface (see *Movie S8*), realizing a droplet transport.<sup>2</sup>

#### 4. CONCLUSIONS

In analogy to the singly re-entrant mushroomlike geometry of springtail cuticles, we designed a flexible water-repelling surface structured with mushroomlike basic units, each unit comprising a mesoscale head and a microscale spring set. Three-dimensional projection microstereolithography was employed in the micro-nano fabrication to rapidly and precisely replicate our design. Our surface was shown to exhibit strong mechanical robustness against ubiquitous normal and shear compression and was even able to endure tribological friction under the load as high as  $0.44 \text{ N mm}^{-1}$ , around  $\sim 11$  times higher than previous studies.<sup>29</sup> The surface also elevated water repellency to impacting droplets by enhancing impalement resistance and reducing contact time. Specifically, the impalement resistance was shown to reach an improvement of  $\sim 80\%$  by triggering structural tilting movements, around  $\sim 5$  times higher than previous studies.<sup>26</sup> Such tilting movements were also applied to repelling obliquely impacting water droplets. We believe this study to be the very first demonstration of flexible interfacial structures to robustly endure tribological friction as well as to promote water repellency, approaching real-world applications of water repelling. Also, by combining different flexibilities in each mushroomlike unit, the resulting flexibility gradient was shown to directionally manipulate droplets, thereby paving the way for droplet transport.

#### ■ ASSOCIATED CONTENT

##### Supporting Information

The Supporting Information is available free of charge at <https://pubs.acs.org/doi/10.1021/acsami.1c10157>.

Some more details about surface design and fabrication, mechanical robustness, static water repellency, kinetic water repellency, droplet transport, and related figures ([PDF](#))

Compression test (*Movie S1*) ([AVI](#))

Contact angle and adhesion (*Movie S2*) ([AVI](#))



Droplets normally impacting mushroomlike units (Movie S3) (AVI)

Droplets normally impacting mushroomlike units at edge (Movie S4) (AVI)

Droplets normally impacting gaps between mushroomlike units (Movie S5) (AVI)

Droplets normally impacting gaps between mushroomlike units at edge (Movie S6) (AVI)

Droplets obliquely impacting mushroomlike flexible units (Movie S7) (AVI)

Droplet transport (Movie S8) (AVI)

## AUTHOR INFORMATION

### Corresponding Authors

**Xi Shi** – State Key Laboratory of Mechanical System and Vibration, Shanghai Jiao Tong University, Shanghai 200240, China; Email: [xishi@sjtu.edu.cn](mailto:xishi@sjtu.edu.cn)

**Zhike Peng** – State Key Laboratory of Mechanical System and Vibration, Shanghai Jiao Tong University, Shanghai 200240, China; [orcid.org/0000-0002-2095-7075](https://orcid.org/0000-0002-2095-7075); Email: [z.peng@sjtu.edu.cn](mailto:z.peng@sjtu.edu.cn)

### Authors

**Songtao Hu** – State Key Laboratory of Mechanical System and Vibration, Shanghai Jiao Tong University, Shanghai 200240, China; [orcid.org/0000-0002-8405-3788](https://orcid.org/0000-0002-8405-3788)

**Tom Reddyhoff** – Department of Mechanical Engineering, Imperial College London, London SW7 2AZ, United Kingdom

**Jinbang Li** – School of Mechanical Engineering and Mechanics, Ningbo University, Ningbo 315211, China

**Xiaobao Cao** – Department of Chemistry and Applied Biosciences, ETH Zurich, Zurich 8093, Switzerland; [orcid.org/0000-0003-2211-2823](https://orcid.org/0000-0003-2211-2823)

**Andrew J. deMello** – Department of Chemistry and Applied Biosciences, ETH Zurich, Zurich 8093, Switzerland

**Daniele Dini** – Department of Mechanical Engineering, Imperial College London, London SW7 2AZ, United Kingdom; [orcid.org/0000-0002-5518-499X](https://orcid.org/0000-0002-5518-499X)

Complete contact information is available at: <https://pubs.acs.org/10.1021/acsami.1c10157>

### Author Contributions

S.H. and T.R. contributed equally to this work.

### Notes

The authors declare no competing financial interest.

## ACKNOWLEDGMENTS

This work was supported by the National Natural Science Foundation of China (12002202), Young Elite Scientist Sponsorship Program of the China Association for Science and Technology, and State Key Laboratory of Mechanical System and Vibration (MSVZD202104).

## REFERENCES

- (1) Schutzius, T. M.; Jung, S.; Maitra, T.; Graeber, G.; Kohme, M.; Poulikakos, D. Spontaneous Droplet Trampoline on Rigid Superhydrophobic Surfaces. *Nature* **2015**, *527*, 82–85.
- (2) Wang, D.; Sun, Q.; Hokkanen, M. J.; Zhang, C.; Lin, F.; Liu, Q.; Zhu, S.; Zhou, T.; Chang, Q.; He, B.; Zhou, Q.; Chen, L.; Wang, Z.; Ras, R. H. A.; Deng, X. Design of Robust Superhydrophobic Surfaces. *Nature* **2020**, *582*, 55–59.

- (3) Sun, Q.; Wang, D.; Li, Y.; Zhang, J.; Ye, S.; Cui, J.; Chen, L.; Wang, Z.; Butt, H.; Vollmer, D.; Deng, X. Surface Charge Printing for Programmed Droplet Transport. *Nat. Mater.* **2019**, *18*, 936–941.

- (4) Lin, Z.; Cheng, G.; Wu, W.; Pradel, K. C.; Wang, Z. Dual-Mode Triboelectric Nanogenerator for Harvesting Water Energy and as a Self-Powered Ethanol Nanosensor. *ACS Nano* **2014**, *8*, 6440–6448.

- (5) Cheng, Q.; Li, M.; Zheng, Y.; Su, B.; Wang, S.; Jiang, L. Janus Interface Materials: Superhydrophobic Air/Solid Interface and Superoleophobic Water/Solid Interface Inspired by a Lotus Leaf. *Soft Matter* **2011**, *7*, 5948–5951.

- (6) Feng, L.; Zhang, Y.; Xi, J.; Zhu, Y.; Wang, N.; Xia, F.; Jiang, L. Petal Effect: a Superhydrophobic State with High Adhesive Force. *Langmuir* **2008**, *24*, 4114–4119.

- (7) Hensel, R.; Neinhuis, C.; Werner, C. The Springtail Cuticle as a Blueprint for Omniphobic Surfaces. *Chem. Soc. Rev.* **2016**, *45*, 323–341.

- (8) Liimatainen, V.; Drotlef, D. M.; Son, D.; Sitti, M. Liquid-Superrepellent Bioinspired Fibrillar Adhesives. *Adv. Mater.* **2020**, *32*, No. 2000497.

- (9) Yun, G.; Jung, W.; Oh, M. S.; Jang, G. M.; Baek, J.; Kim, N. I. I.; Im, S. G.; Jung, H. Springtail-Inspired Superomniphobic Surface with Extreme Pressure Resistance. *Sci. Adv.* **2018**, *4*, No. eaat4978.

- (10) Liu, X.; Gu, H.; Wang, M.; Du, X.; Gao, B.; Elbaz, A.; Sun, L.; Liao, J.; Xiao, P.; Gu, Z. 3D Printing of Bioinspired Liquid Superrepellent Structures. *Adv. Mater.* **2018**, *30*, No. 1800103.

- (11) Li, J.; Qin, Q.; Shah, A.; Ras, R. H. A.; Tian, X.; Jokinen, V. Oil Droplet Self-Transportation on Oleophobic Surfaces. *Sci. Adv.* **2016**, *2*, No. e1600148.

- (12) Kim, J. H.; Shim, T. S.; Kim, S. Lithographic Design of Overhanging Microdisk Arrays Toward Omniphobic Surfaces. *Adv. Mater.* **2016**, *28*, 291–298.

- (13) Liu, T.; Kim, C. Turning a Surface Superrepellent Even to Completely Wetting Liquids. *Science* **2014**, *346*, 1096–1100.

- (14) Hensel, R.; Finn, A.; Helbig, R.; Braun, H.; Neinhuis, C.; Fischer, W.; Werner, C. Biologically Inspired Omniphobic Surfaces by Reverse Imprint Lithography. *Adv. Mater.* **2014**, *26*, 2029–2033.

- (15) Tuteja, A.; Choi, W.; Mabry, J. M.; McKinley, G. H.; Cohen, R. E. Robust Omniphobic Surfaces. *Proc. Natl. Acad. Sci. U.S.A.* **2008**, *105*, 18200–18205.

- (16) Tuteja, A.; Choi, W.; Ma, M.; Mabry, J. M.; Mazzella, S. A.; Rutledge, G. C.; McKinley, G. H.; Cohen, R. E. Designing Superoleophobic Surfaces. *Science* **2007**, *318*, 1618–1622.

- (17) Richard, D.; Clanet, C.; Quere, D. A Contact Time of a Bouncing Drop. *Nature* **2002**, *417*, 811.

- (18) Hu, S.; Reddyhoff, T.; Puhan, D.; Vladescu, S.-C.; Shi, X.; Dini, D.; Peng, Z. Droplet Manipulation of Hierarchical Steel Surfaces Using Femtosecond Laser Fabrication. *Appl. Surf. Sci.* **2020**, *521*, No. 146474.

- (19) Song, M.; Liu, Z.; Ma, Y.; Dong, Z.; Wang, Y.; Jiang, L. Reducing the Contact Time Using Macro Anisotropic Superhydrophobic Surfaces - Effect of Parallel Wire Spacing on the Drop Impact. *NPG Asia Mater.* **2017**, *9*, No. e415.

- (20) Gauthier, A.; Symon, S.; Clanet, C.; Quere, D. Water Impacting on Superhydrophobic Macrottextures. *Nat. Commun.* **2015**, *6*, No. 8001.

- (21) Liu, Y.; Andrew, M.; Li, J.; Yeomans, J. M.; Wang, Z. Symmetry Breaking in Drop Bouncing on Curved Surfaces. *Nat. Commun.* **2015**, *6*, No. 10034.

- (22) Bird, J. C.; Dhiman, R.; Kwon, H.; Varanasi, K. K. Reducing the Contact Time of a Bouncing Drop. *Nature* **2013**, *503*, 385–388.

- (23) Chantelot, P.; Coux, M.; Clanet, C.; Quere, D. Drop Trampoline. *Europhys. Lett.* **2018**, *124*, 24003.

- (24) Kim, J.; Rothstein, J. P.; Shang, J. K. Dynamics of a Flexible Superhydrophobic Surface during a Drop Impact. *Phys. Fluids* **2018**, *30*, No. 072102.

- (25) Vasileiou, T.; Gerber, J.; Prautzsch, J.; Schutzius, T. M.; Poulikakos, D. Superhydrophobicity Enhancement through Substrate Flexibility. *Proc. Natl. Acad. Sci. U.S.A.* **2016**, *113*, 13307–13312.

- (26) Hu, S.; Cao, X.; Reddyhoff, T.; Puhan, D.; Vladescu, S.-C.; Wang, J.; Shi, X.; Peng, Z.; deMello, A. J.; Dini, D. Liquid Repellency Enhancement through Flexible Microstructures. *Sci. Adv.* **2020**, *6*, No. eaba9721.

(27) Wang, L.; Gao, C.; Hou, Y.; Zheng, Y.; Jiang, L. Magnetic Field-Guided Directional Rebound of a Droplet on a Superhydrophobic Flexible Needle Surface. *J. Mater. Chem. A* **2016**, *4*, 18289–18293.

(28) Wang, L.; He, Z.; Ding, Y.; Zhou, X.; Liu, J. The Rebound Motion of Liquid Metal Droplet on Flexible Micro/Nano Needle Forest. *Adv. Mater. Interfaces* **2016**, *3*, No. 1600008.

(29) Hu, S.; Cao, X.; Reddyhoff, T.; Puhan, D.; Vladescu, S.-C.; Wang, Q.; Shi, X.; Peng, Z.; deMello, A. J.; Dini, D. Self-Compensating Liquid-Repellent Surfaces with Stratified Morphology. *ACS Appl. Mater. Interfaces* **2020**, *12*, 4174–4182.

(30) Xiang, Y.; Huang, S.; Huang, T.; Dong, A.; Cao, D.; Li, H.; Xue, Y.; Lv, P.; Duan, H. Superrepellency of Underwater Hierarchical Structures on Salvinia Leaf. *Proc. Natl. Acad. Sci. U.S.A.* **2020**, *117*, 2282–2287.

(31) Feng, S.; Delannoy, J.; Malod, A.; Zheng, H.; Quere, D.; Wang, Z. Tip-induced Flipping of Droplets on Janus Pillars: From Local Reconfiguration to Global Transport. *Sci. Adv.* **2020**, *6*, No. eabb4540.

(32) Tian, X.; Verho, T.; Ras, R. H. A. Moving Superhydrophobic Surfaces toward Real-World Applications. *Science* **2016**, *352*, 142–143.

(33) Hoshian, S.; Jokinen, V.; Somerkivi, V.; Lokanathan, A. R.; Franssila, S. Robust Superhydrophobic Silicon without a Low Surface-Energy Hydrophobic Coating. *ACS Appl. Mater. Interfaces* **2015**, *7*, 941–949.

(34) Jin, H.; Tian, X.; Ikkala, O.; Ras, R. H. A. Preservation of Superhydrophobic and Superoleophobic Properties upon Wear Damage. *ACS Appl. Mater. Interfaces* **2013**, *5*, 485–488.

(35) Rioboo, R.; Voue, M.; Adao, H.; Conti, J.; Vaillant, A.; Seveno, D.; De Coninck, J. Drop Impact on Soft Surfaces: Beyond the Static Contact Angles. *Langmuir* **2010**, *26*, 4873–4879.

(36) Soto, D.; De Larivière, A. B.; Boutillon, X.; Clanet, C.; Quere, D. The Force of Impacting Rain. *Soft Matter* **2014**, *10*, 4929–4934.

(37) Liu, Y.; Moevius, L.; Xu, X.; Qian, T.; Yeomans, J. M.; Wang, Z. Pancake Bouncing on Superhydrophobic Surfaces. *Nat. Phys.* **2014**, *10*, 515–519.